



## OPEN

SUBJECT AREAS:  
SPINTRONICS  
MAGNETIC DEVICESReceived  
8 July 2014Accepted  
3 October 2014Published  
30 October 2014Correspondence and  
requests for materials  
should be addressed to  
H.Y. (haiming.yu@  
buaa.edu.cn) or D.G.  
(grundler@ph.tum.de)\* Current address:  
Spintronics  
Interdisciplinary  
Center, Beihang  
University, Department  
of Electrical  
Engineering, Beihang  
University.

# Magnetic thin-film insulator with ultra-low spin wave damping for coherent nanomagnonics

Haiming Yu<sup>1\*</sup>, O. d'Allivy Kelly<sup>2</sup>, V. Cros<sup>2</sup>, R. Bernard<sup>2</sup>, P. Bortolotti<sup>2</sup>, A. Anane<sup>2</sup>, F. Brandl<sup>1</sup>, R. Huber<sup>1</sup>, I. Stasinopoulos<sup>1</sup> & D. Grundler<sup>1,3</sup><sup>1</sup>Physik Department E10, Technische Universität München, James-Frank-Strasse 1, D-85748 Garching b. München, Germany,<sup>2</sup>Unité Mixte de Physique CNRS/Thales and Université Paris-Sud, 1 avenue Augustin Fresnel, Palaiseau, France, <sup>3</sup>Institut des Matériaux, École Polytechnique Fédérale de Lausanne, 1015 Lausanne, Switzerland.

Wave control in the solid state has opened new avenues in modern information technology.

Surface-acoustic-wave-based devices are found as mass market products in 100 millions of cellular phones. Spin waves (magnons) would offer a boost in today's data handling and security implementations, i.e., image processing and speech recognition. However, nanomagnonic devices realized so far suffer from the relatively short damping length in the metallic ferromagnets amounting to a few 10 micrometers typically. Here we demonstrate that nm-thick YIG films overcome the damping chasm. Using a conventional coplanar waveguide we excite a large series of short-wavelength spin waves (SWs). From the data we estimate a macroscopic damping length of about 600 micrometers. The intrinsic damping parameter suggests even a record value about 1 mm allowing for magnonics-based nanotechnology with ultra-low damping. In addition, SWs at large wave vector are found to exhibit the non-reciprocal properties relevant for new concepts in nanoscale SW-based logics. We expect our results to provide the basis for coherent data processing with SWs at GHz rates and in large arrays of cellular magnetic arrays, thereby boosting the envisioned image processing and speech recognition.

The insulating ferrimagnet yttrium iron garnet (YIG) has recently attracted considerable interest in both spintronics<sup>1–3</sup> and spin caloritronics<sup>4–7</sup>. One reason is that bulk and micrometer-thick YIG offers the smallest possible damping parameter  $\alpha$  for spin waves (SWs) in the GHz frequency regime. The value of  $\alpha$  amounts to about  $5 \times 10^{-5}$  and is two orders of magnitude smaller compared to the best metallic magnets<sup>9,10</sup>. At the same time the research field of magnonics has evolved rapidly based on nanostructured metals<sup>11</sup>. In magnonics one aims at the transmission, storage and processing of information using propagating and interfering spin waves (SWs)<sup>12</sup>. A small damping parameter  $\alpha$  is key for magnonic crystals<sup>13</sup> and spin wave logic devices based on interference effects<sup>14,15</sup>. Advanced concepts are based on coherent SW processing in cellular non-linear networks and magnonic holography memory<sup>14,16</sup> creating also a demand for SWs that can propagate over large distances i.e., possessing large attenuation (decay) lengths. Nonreciprocal SW properties<sup>17–19</sup> thoroughly studied in YIG and the metal Permalloy ( $\text{Ni}_{80}\text{Fe}_{20}$ ) allow one to implement alternative ways for spin wave logic applications<sup>20,21</sup>. The relatively small attenuation length  $l_d$  of only a few 10  $\mu\text{m}$  found in metallic ferromagnets<sup>22</sup> hinders however such developments. Magnonic nanodevices from the insulator YIG would be ground-breaking but have yet been elusive as relevant films with low damping needed to be micrometer thick<sup>12</sup>. Very recently, Liu et al.<sup>23</sup> studied ferromagnetic resonance of YIG films with a thickness of 7 to 26 nm finding a promising damping constant  $\alpha$  of 0.001. This value is already a factor of about three better than metallic ferromagnets used in magnonics. Hahn et al. showed that the damping constant is unaffected when nanostructuring ultra-thin YIG films<sup>24</sup>. Pirro et al.<sup>25</sup> studied a 100 nm thick YIG thin film and observed a spin-wave decay length  $l_d$  of 31  $\mu\text{m}$ . Here we report propagating spin waves in a 20 nm-thick YIG film exhibiting a damping parameter of  $2.3 \times 10^{-4}$ . We estimate a decay length of 580  $\mu\text{m}$  from our data surpassing  $l_d$  of metallic ferromagnets by an order of magnitude or even more. We explore spin wave modes with nine different wavelengths  $\lambda$  down to 560 nm. The group velocities  $v_g$  are found to vary between 0.6 km/s and 1.2 km/s depending on the wave vector and applied magnetic field  $H$ . The nonreciprocity is found to increase with increasing wavevector  $k = 2\pi/\lambda$  and is thus promising in view of nanoscale spin-wave logic devices. Our experimental work demonstrates that the thin-film magnetic insulator YIG allows

one to overcome the damping problem for nanomagnonics and to boost further developments in magnonic circuit technology for information processing at GHz operational frequencies.

## Results

**Spin-wave propagation in 20-nm-thick YIG.** Figure 1a shows the sketch of a thin-film YIG mesa with two integrated coplanar waveguides (CPWs).

To measure spin-wave propagation, we connected a vector network analyzer (VNA) to the CPWs that provided a microwave current  $i_{rf}$  at GHz frequencies  $f$ . The inhomogeneous microwave magnetic field  $\mathbf{h}_{rf}$  exerted a torque on the magnetic moments generating spin waves with a characteristic wave-vector distribution  $I(k)^{26}$ .  $I(k)$  calculated from  $i_{rf}$  (see section ‘Methods’) is shown in Fig. 1b and contains a main excitation at  $k_1$ , and several higher-order excitations at  $k_2, k_3, k_4, k_5$  and  $k_6$ . The wave vectors  $k_i$  are perpendicular to the CPW ( $i = 1, 2, 3, \dots$ ). We measured both reflection ( $S_{11}, S_{22}$ ) and transmission signals with spin waves propagating in the opposing directions, namely  $S_{12}$  and  $S_{21}$ <sup>27</sup>. In Fig. 1c we show a spectrum  $S_{12}$  taken on a 20 nm thick YIG film subject to an in-plane field  $H$  of  $\mu_0 H = -2$  mT. The field was collinear with the CPWs and larger than the reversal field (see below). Thus Damon-Eshbach-type (DE) modes were excited with  $k$  being perpendicular to the magnetization  $\mathbf{M}$ . To extract the transmitted spin-wave contribution we subtracted a spectrum  $S_{12}$  from all data that was taken at  $-100$  mT under an angle  $\theta$  of 0 deg. We depict the imaginary part of the transmission signal. As a function of frequency  $f$  we observe a series of oscillating signatures indicating spin-wave propagation between CPW1 and CPW2. The most prominent transmission signal is around 0.76 GHz, a second mode at about 1.05 GHz, a third mode at about 1.32 GHz, etc. These values of  $f$  are extracted from the

extrema of envelope functions that connect local maxima of the oscillations labeled by  $k_1, k_2, \dots$ . With increasing eigenfrequency the signal strengths are found to diminish in a similar manner as expected from the distribution of excitations strengths  $I(k)$  shown in Fig. 1b. The highest  $k$  vector we detected out of the noise level is the mode  $k_7$  (not shown). When we vary the field strength  $H$  the eigenfrequencies  $f$  shift with  $H$  (Fig. 1d) as one would expect from the Landau-Lifshitz equation. The thin YIG film is a soft magnetic material exhibiting a reversal field of about 0.5 mT in Fig. 1d.

We find that signal strengths of the oscillating signatures are different for positive and negative fields. The discrepancy between  $+H$  and  $-H$  spectra depends on the frequency. A similar signal-strength discrepancy is found between spectra  $S_{12}$  and  $S_{21}$  taken at one-and-the-same magnetic field. This is highlighted in the inset of Fig. 1c where spectra  $S_{12}$  (red line) and  $S_{21}$  (black line) are compared for an applied field of  $-2$  mT. We attribute the different signal strengths to a wave-vector dependent nonreciprocity that will be detailed below.

The modes observed in  $S_{12}$  of Fig. 1c and 1d suggest a one-to-one correspondence with different  $k$  vectors of the CPW excitation distribution  $I(k)$  shown in Fig. 1b. This is substantiated in Fig. 2a. Here we show the resonance frequencies  $f$  extracted at 5 mT from extrema of the relevant envelope functions as a function of wave vector  $k$ . For the square symbols we used Fig. 1b to attribute the eigenfrequencies  $f$  to specific values of  $k$ . For the two further resonances marked by  $k_2'$  and  $k_4'$  we used  $I(k)$  provided by the out-of-plane component of  $\mathbf{h}_{rf}$  (shown in the section ‘Methods’). The series of measured spin-wave frequencies follows a characteristic wave-vector dependence. Using the formalism of Kalinikos and Slavin<sup>28</sup> we have calculated a spin-wave dispersion relation  $f(k)$  using the following parameters for the 20 nm thick YIG film: saturation magnetization  $M_s = 0.176$  T taken from Ref. 29, exchange constant  $0.192 \times 10^{-6}$  erg/cm<sup>30</sup>,  $\mu_0 H = 5$  mT and  $\theta = 0$  deg. The theoretical curve (solid line) quantitatively remodels the measured data substantiating our mode allocation. We conclude that spin waves are excited by both in-plane and out-of-plane components of the CPW exhibiting wave vectors ranging from about

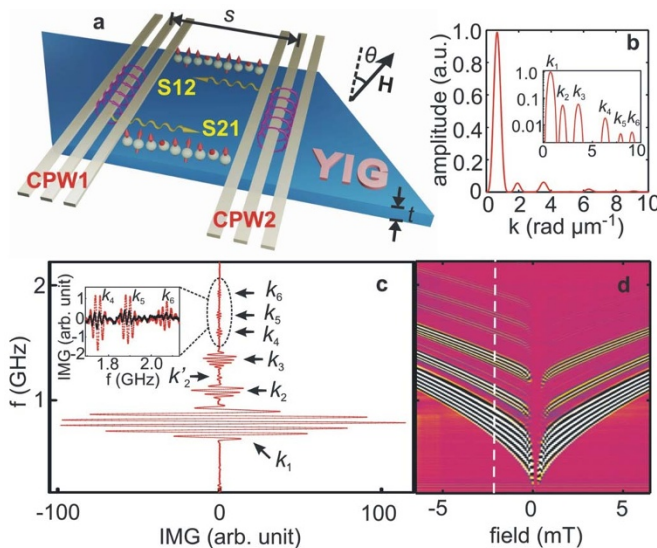


**Figure 1** | (a) Sketch of the YIG film with integrated CPWs. The microwave magnetic field  $\mathbf{h}_{rf}$  (circles) and the different spin-wave propagation directions are indicated. (b) Excitation spectrum  $I(k)$  obtained by Fourier transformation of  $i_{rf}$  (in-plane component). The inset shows the same chart with a logarithmic  $y$ -axis scale in order to highlight higher-order modes. (c) Spin wave spectrum of  $S_{12}$  (transmission), meaning spin waves were excited at CPW2 and detected at CPW1. The applied in-plane field amounted to  $-2$  mT ( $\theta = 0$ , parallel to CPW lines). In the inset we compare spectra  $S_{12}$  (red line) and  $S_{21}$  (black line) taken at  $-2$  mT. (d) Color-coded spectra of spin-wave propagation data  $S_{12}$  as a function of  $H$  ( $\theta = 0$ ). The spectrum shown in (c) is extracted from the white dotted line in (d). The coercive (reversal) field is about 0.5 mT.

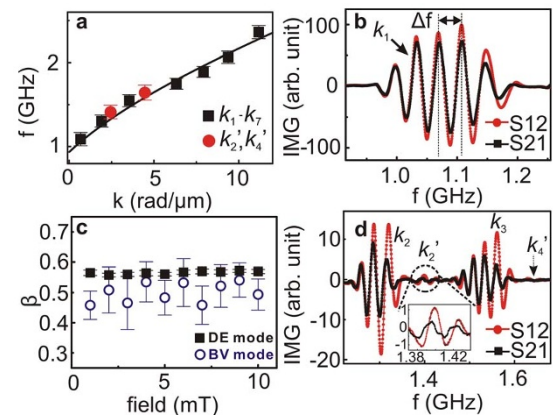


**Figure 2** | (a) Calculated dispersion relation  $f(k)$  (line) compared to experimentally observed eigen-frequencies at 5 mT (symbols). Squares (circles) indicate eigenfrequencies attributed to wave vectors from  $k_1$  to  $k_7$  ( $k_2'$  and  $k_4'$ ). (b) Spin wave spectra of mode  $k_1$  extracted from transmission data  $S_{21}$  (black squares) and  $S_{12}$  (red circles) taken at 5 mT. Amplitudes are different attributed to nonreciprocity. From the frequency separation  $\Delta f$  we calculate the group velocity. (c) Nonreciprocity parameter  $\beta$  as a function of applied field calculated for the mode  $k_1$  from transmission data of  $S_{12}$  and  $S_{21}$ . The black squares represent the DE mode ( $\theta = 0$ ), and the open blue dots are for the BV mode ( $\theta = 90$  deg). (d) Spin wave spectra of  $k_2$  and  $k_3$  modes extracted from  $S_{21}$  (red circles) and  $S_{12}$  (black squares) transmission data at 5 mT. Modes attributed to the out-of-plane field component of  $\mathbf{h}_{rf}$  are marked by a prime. The inset enlarges the signal near  $k_2'$ .



1.0 to 11.2 rad/ $\mu\text{m}$ . One-and-the-same CPW excites  $k$  values that vary by one order of magnitude. The shortest wavelength amounts to  $\lambda = 2\pi/k = 560$  nm, coming close to the minimum wavelength of 365 nm that was reported recently for a nanostructured magnonic grating coupler based on metallic ferromagnets<sup>31</sup>. Note however that we use a conventional CPW to generate such short-wavelength SWs. We now investigate in detail the signal-strength discrepancies observed for positive and negative fields.

**Analysis of propagating spin waves: nonreciprocity.** By comparing both transmission data  $S_{12}$  at different fields (inset of Fig. 1c) as well as  $S_{12}$  and  $S_{21}$  taken at the same field (Fig. 2b) we clearly observe discrepancies in the mode intensities for both scenarios. Such variations are known as the nonreciprocity effect when exciting spin waves. Two different microscopic origins have been discussed for nonreciprocal properties of spin waves in YIG with  $\mathbf{k}$  being perpendicular to  $\mathbf{M}$ , i.e., the intrinsically nonreciprocal character of the DE surface mode<sup>12</sup> and the excitation characteristics given by an antenna<sup>19,32</sup>. Using a very thin YIG film we do not consider the first reason to be relevant and attribute the experimentally observed nonreciprocity to the CPW consistent with Refs. 19, 32. For the following analysis we define and evaluate the nonreciprocity parameter  $\beta$  and decay length  $l_d$  using the following set of reference<sup>33</sup>:

$$a_{21} = \beta a_{11} \exp(-s/l_d);$$

$$a_{12} = (1 - \beta) a_{22} \exp(-s/l_d) \Rightarrow \beta = \frac{\frac{a_{21}}{a_{11}}}{\frac{a_{21}}{a_{11}} + \frac{a_{12}}{a_{22}}} \Rightarrow l_d = \frac{-s}{\ln\left(\frac{a_{21}}{\beta a_{11}}\right)} \quad (1)$$

where  $l_d$  is the same for counter-propagating spin waves in a given magnetic state. Following equation (1) the value  $\beta = 0.5$  indicates reciprocal characteristics. The signal amplitudes  $a_{uv}$  are extracted from the peak-to-peak variation in the imaginary part of the spectra  $S_{uv}$  where  $u, v = 1, 2$  label the CPW and port of the VNA.

In Fig. 2c we show parameters  $\beta$  evaluated for the DE mode labelled with  $k_1$  (full symbols). For  $1 \text{ mT} \leq \mu_0 H \leq 10 \text{ mT}$  we find an almost constant  $\beta$  between about 0.55 and 0.58. These values close to 0.5 indicate a weak nonreciprocity. When the field  $H$  is applied at  $\theta = 90^\circ$  to rotate  $\mathbf{M}$ , the CPWs excite spin-wave modes in the backward volume magnetostatic spin wave mode (BV mode) configuration. The propagation signal (not shown) is weaker due to the small torque by  $\mathbf{h}_{\text{rf}}$  acting on the spins. For such modes, we evaluate the nonreciprocity parameter  $\beta$  as shown by open symbols in Fig. 2c. Despite the larger error bar,  $\beta$  is found to be smaller compared to the DE mode and around 0.5. This suggests reciprocal behavior. The absence of nonreciprocity for the BV mode is expected as  $\mathbf{M}$  does not possess a component being perpendicular to  $\mathbf{k}$ <sup>32,34</sup>.

**Spin waves with different wave vectors.** Figure 2d shows spin wave transmission spectra for  $\theta = 0^\circ$  deg with an applied field of 5 mT for larger DE-mode wave vectors  $k$ . Compared to the  $k_1$  mode shown in Fig. 2b, the difference between  $S_{21}$  (red) and  $S_{12}$  (black) is more prominent and indicates a larger nonreciprocity effect. We find  $\beta$  to vary from mode  $k_1$  to  $k_6$  ( $k_2$ ). In Fig. 3a, we summarize  $\beta$  for modes with different vectors  $k$  observed at 5 mT. We find an increase of  $\beta$  from about 0.56 to 0.79 with increasing  $k$ . An analytical model for the spin wave nonreciprocity was given in Ref. 32,

$$a_{\pm} = \frac{f}{\gamma} \pm \frac{1}{M_s} \left( H^2 - \frac{f^2}{\gamma^2} \right) \quad (2)$$

where  $a_{\pm}$  indicates the spin wave amplitude of positive (+) and negative (−) propagating direction.  $\gamma$  is the gyromagnetic ratio. Since YIG has a low saturation magnetization  $M_s$ , a pronounced nonreciprocity can result from equation (2). Using the dispersion relation  $f(k)$  shown in Fig. 2a, we evaluate  $\beta$  in that we consider the

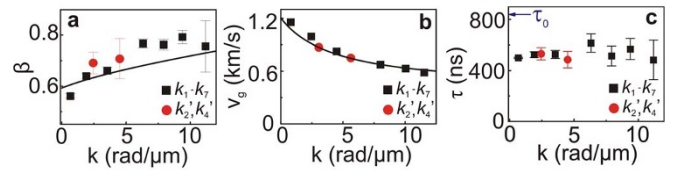


**Figure 3** | (a) Nonreciprocity parameter  $\beta$  calculated for different vectors  $k$  from transmission data. Black squares show CPW excitation from  $k_1$  to  $k_7$  modes. Red dots show out-of-plane component CPW excitations. The black line is the calculated curve using equations (1) and (2) and  $f(k)$  from Fig. 2a. (b) Group velocity of DE spin waves with different vectors  $k$ . The line indicates the group velocity calculated from the dispersion relation in Fig. 2a. (c) Spin wave relaxation time calculated from equation (4) using experimental data. The arrow indicates the value  $\tau_0$  calculated from the damping parameter  $\alpha$  using equation (5). All data are for  $\mu_0 H = 5$  mT. Black squares show CPW excitation from  $k_1$  to  $k_7$  modes. Red dots show out-of-plane component CPW excitations.

relevant spin-precessional frequency  $f$  for the different  $k$  in equation (2). The evaluation is depicted by the solid line in Fig. 3a. The calculated dependency explains the more pronounced nonreciprocity observed for large  $k$  vectors. Thin YIG films thus seem to be particularly interesting for nonreciprocity-based logic<sup>20</sup> using spin waves with large values of  $k$ , i.e., short wavelengths. Thin YIG thus offers such devices with nanoscale dimensions.

**Spin-wave propagation velocities, linewidth and relaxation.** Following Refs. 27, 35, the frequency separation  $\Delta f$  (indicated in Fig. 2b) reflects a change in the phase by  $2\pi$  which is accumulated by spin waves propagating along  $s$  between the inner conductors of CPW1 and CPW2. The group velocity  $v_g$  is calculated from  $\Delta f$  according to<sup>27</sup>

$$v_g = \frac{\partial \omega}{\partial k} \approx \frac{2\pi \Delta f}{2\pi/s} = \Delta f \cdot s, \quad (3)$$

where  $s = 30 \mu\text{m}$  is the distance between two CPW signal lines as indicated in Fig. 1a. We find that the spin wave group velocity decreases from 1.16 to 0.59 km/s with increasing  $k$ . When we calculate the group velocity from the theoretical dispersion relation  $f(k)$  using  $v_g = \frac{2\pi df}{dk}$  we remodel well the observed large variation (line in Fig. 3b).

We observe a finite broadening  $\delta k$  for each excitation peak in Fig. 1b. E.g., mode  $k_1$  has a width  $\delta k$  of around 0.5 rad/ $\mu\text{m}$ . From this we estimate the effective linewidth  $\delta f = v_g \delta k / 2\pi$  (in reflection geometry)<sup>26</sup> to be about 80 MHz at 5 mT ( $v_g = 1$  km/s). This value is close to what we observe in the experiment. It is much larger than the intrinsic linewidth of about 15 MHz calculated from the damping parameter  $\alpha$ <sup>29</sup>. The linewidth  $\delta f$  of the reflection spectrum (see section ‘Methods’) thus does not provide the intrinsic linewidth but indicates the finite  $k$  distribution from CPW excitation.

We now investigate the spin wave decay length  $l_d$  and relaxation time  $\tau$ . To estimate the decay length of spin waves, we use the last line of equation (1) considering  $\beta$  from the previous section. We obtain a decay length of 580  $\mu\text{m}$  for  $k_1$  with  $\mu_0 H = 5$  mT in DE mode. A large decay length is essential for spin wave logic device applications<sup>36</sup>. Using extracted decay lengths  $l_d$  (Fig. 4a in section ‘Methods’) and the group velocities  $v_g$  of Fig. 3b, we calculate spin relaxation times  $\tau$  by

$$\tau = \frac{l_d}{v_g}. \quad (4)$$

The results are shown in Fig. 3c. We find that the observed spin relaxation times vary slightly between 480 ns and 620 ns depending



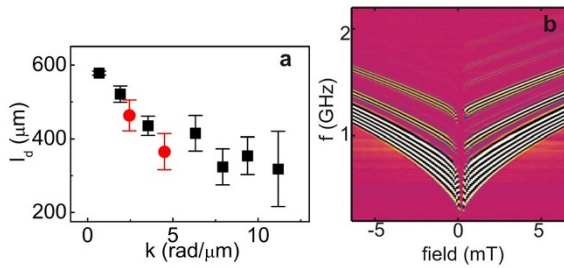


**Figure 4** | (a) Decay lengths  $l_d$  extracted at 5 mT from measured scattering parameters and the data of Fig. 3a according to equation (1). (b) Color-coded plot of spin-wave propagation data of  $S_{21}$  as a function of  $H$  ( $\theta = 0$ ). The spin waves are excited at CPW1 and detected at CPW2.

on  $k$ . These values are compared to the expected relaxation time  $\tau_0$  estimated from  $\alpha = 2.3 \times 10^{-4}$  given in Ref. 29 according to

$$\tau_0 = \frac{1}{2\pi\alpha f_0}, \quad (5)$$

where  $f_0$  is the eigenfrequency of the uniform precession ( $k = 0$ )<sup>37</sup>.  $f_0$  is extracted from the calculated dispersion relation shown in Fig. 2a at  $k = 0$ . We get  $\tau_0 = 840$  ns from equation (5). In the denominator of equation (5) we did not introduce the ellipticity factor  $P_A$  ( $P_A \leq 1$ )<sup>37</sup>. Thereby we obtained the lower limit of  $\tau_0$ . The factor  $P_A$  was not known as we did not measure field-dependent eigenfrequencies at  $k = 0$  (uniform precession).

Our best decay length of 580  $\mu\text{m}$  is more than 18 times larger than the value of 31  $\mu\text{m}$  reported for 100 nm thick YIG by Pirro et al.<sup>25</sup>. The authors found a similar velocity  $v_g$  of  $\approx 1.1$  km/s. In their studies the authors deposited however Pt on top of the YIG and thereby increased the damping parameter  $\alpha$  by a factor of 5.4. Compared to our best value they performed their experiment at a frequency  $f_0$  that was larger by a factor of 3.5 suggesting a further reduction in  $\tau$  according to equation (5). The total reduction factor of  $5.4 \times 3.5 \approx 19$  thus explains the smaller value  $l_d = v_g\tau = 31$   $\mu\text{m}$  found in their case. The values  $\tau$  that we obtained experimentally from the spin-wave transmission between CPW1 and CPW2 were smaller than the expected  $\tau_0$ . We attribute the smaller  $\tau$  to a reduced spin-wave attenuation length  $l_d$  provoked partly by the metallic ground leads that reside between the two relevant signal lines for excitation and detection. The ground lines are expected to modify the spin-wave properties locally<sup>38</sup> and thereby induce either partial reflection or additional damping. The experimentally extracted values  $\tau$  of Fig. 3c are therefore expected to underestimate the real relaxation time. Using  $\tau_0 = 840$  ns and  $v_g = 1.16$  km/s the theoretically expected decay length  $l_d = v_g\tau$  amounts to 970  $\mu\text{m}$  at  $k = 1$  rad/

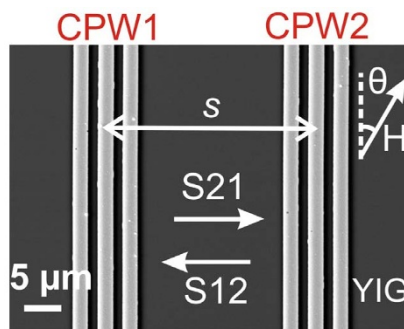


**Figure 5** | SEM image of the integrated CPWs on the YIG thin film. The parameter  $s$  indicates the propagation distance being 30  $\mu\text{m}$ . The propagation directions of  $S_{12}$  and  $S_{21}$  are indicated. The angle  $\theta$  of the applied field is defined.

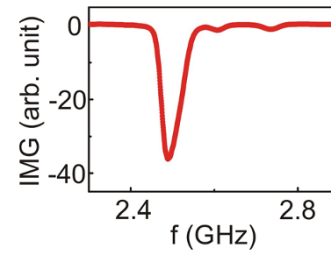


**Figure 6** | Spectrum  $S_{11}$  taken in reflection configuration using one-and-the-same CPW at 30 mT ( $\theta = 0$ ). The imaginary part of the signal is shown.

$\mu\text{m}$ . Transmission lines that in particular avoid the ground lines might be appropriate to observe directly the macroscopic  $l_d$  of about 1 mm predicted by  $\alpha = 2.3 \times 10^{-4}$ .

In conclusion, we have shown that SWs excited in nm-thick YIG films exhibit a pronounced wave-vector-dependent nonreciprocity and a record decay length for a thin-film magnonic material. The findings are expected to boost the coherent processing of spin waves in integrated Mach-Zehnder interferometers, magnetic cellular networks and magnonic holographic memories.

## Methods

**Sample fabrication.** We grow thin YIG films on Gadolinium Gallium Garnet (111) substrates using Pulsed Laser Deposition. Growth temperature is set to be 650°C, and oxygen pressure to 0.25 mbar. The YIG thickness is measured using X-ray reflectometry. RMS roughness is better than 0.5 nm. The Gilbert damping parameter is as low as  $2.3 \times 10^{-4}$ <sup>29</sup>. We used e-beam lithography to form a mesa with 45 degree edges as shown in Fig. 1a to avoid reflection of the spin waves. The width of the mesa was 300  $\mu\text{m}$ . We used Ar milling to etch away the YIG film around the mesa area. After etching, we measured the step at the edge of the mesa being 40 nm, and all the YIG film (20 nm thick) have been therefore etched away. Using again e-beam lithography, coplanar wave guides (CPWs) were integrated on the YIG mesa to perform broadband spin-wave spectroscopy (Fig. 4b). Figure 5 shows a Scanning Electron Microscope (SEM) image of two CPWs with a YIG thin film underneath. These CPWs were designed identically having 2.1  $\mu\text{m}$  wide signal lines and ground lines and 1.4  $\mu\text{m}$  wide gaps between them. The distance  $s$  between two central conductors of adjacent CPWs was 30  $\mu\text{m}$ .

**Spin-wave absorption spectrum.** We measured absorption spectra in reflection configuration using the scattering parameters  $S_{11}$  or  $S_{22}$ . Figure 6 shows a typical spectrum  $S_{11}$ . The most prominent signal originates from the main excitation of the CPW, i.e. mode  $k_1$ . The two weaker ones result from  $k_2$  and  $k_3$ . The linewidth of the signal  $k_1$  is mainly caused by the broadening  $\delta k$  seen in  $I(k)$  of Fig. 1b near  $k_1$ . The linewidth (full width at half maximum)  $\delta f$  of the prominent resonance amounts to about 60 MHz in Fig. 6.

**Spin wave propagation.** Figure 4b shows the spin wave transmission data for  $S_{21}$ . We used measured scattering parameters and evaluated the decay length  $l_d$  following equation (1) (Fig. 4a). These data entered the calculation of  $\tau$  (Fig. 3c) according to equation (4).

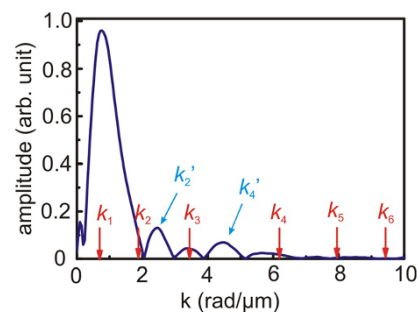


**Figure 7** | Red vertical arrows indicate in-plane  $k$  vectors that are relevant for excitations  $k_1$  to  $k_6$  and have been calculated following Refs. 39, 40. The two tilted blue arrows indicate an appreciable excitation strength at wave vectors  $k_2'$  and  $k_4'$  provided by the simulated out-of-plane component of the radiofrequency field  $\mathbf{h}_{\text{rf}}$ .



The wave vector distribution  $I(k)$  for the in-plane magnetic field component of  $h_{\text{rf}}$  was extracted following Refs. 39, 40. The authors assumed a homogeneous current density in the signal line and counter-flowing shielding currents in the two ground lines of half the amplitude.  $I(k)$  was extracted from the Fourier transformation of this current profile. In our work the microwave frequencies were relatively small and below 2.5 GHz. The Au leads were only 2.1  $\mu\text{m}$  wide, i.e., on the order of the skin depth at small frequencies. As a consequence we assumed the skin effect to be weak<sup>40</sup> and a homogeneous current density to be a reasonable assumption. The authors of Refs. 39, 40 did not provide a formalism for out-of-plane components. Hence for  $I(k')$  representing the out-of-plane component (Fig. 7) we considered the Fourier transformation of a magnetic field distribution provided by the electromagnetic simulation code CST (Computer Simulation Technology for 3-D electromagnetic simulation) used in Ref. 40. We found that some excitation peaks (here at  $k_2$  and  $k_4$ ) did not coincide with the calculated in-plane wave vectors  $k_i$ . Considering that the out-of-plane fields yield a smaller excitation strength compared to in-plane components<sup>39,40</sup> we interpreted the two significantly smaller signals lying between features attributed to  $k_i$  in Fig. 2d as excitations at  $k_2$  and  $k_4$ . The discrepancy for  $k_1$  between the approximation and electromagnetic simulations is reported to be about 10–15% for a small inner conductor width of the CPW<sup>39,40</sup>. Further simulations suggest that the maximum discrepancy occurs for  $k_3$  and is up to about 37%. To quantify wave vectors in the experiment time and spatially resolved magneto-optical microscopy would be relevant<sup>22</sup>.

1. Kajiwar, Y. *et al.* Transmission of electrical signals by spin-wave interconversion in a magnetic insulator. *Nature* **464**, 262–266 (2010).
2. Kurebayashi, H. *et al.* Controlled enhancement of spin-current emission by three-magnon splitting. *Nature Mater.* **10**, 660–664 (2011).
3. Heinrich, B. *et al.* Spin Pumping at the Magnetic Insulator (YIG)/Normal Metal (Au) Interfaces. *Phys. Rev. Lett.* **107**, 066604 (2011).
4. Weiler, M. *et al.* Local Charge and Spin Currents in Magnetothermal Landscapes. *Phys. Rev. Lett.* **108**, 106602 (2012).
5. Uchida, K. *et al.* Spin Seebeck insulator. *Nature Mater.* **9**, 894–897 (2010).
6. Padrón-Hernández, E., Azevedo, A. & Rezende, S. M. Amplification of spin waves by thermal spin-transfer torque. *Phys. Rev. Lett.* **107**, 197203 (2011).
7. Qu, D., Huang, S. Y., Hu, J., Wu, R. & Chien, C. L. Intrinsic Spin Seebeck Effect in Au/YIG. *Phys. Rev. Lett.* **110**, 067206 (2013).
8. Sun, Y. *et al.* Damping in Yttrium Iron Garnet Nanoscale Films Capped by Platinum. *Phys. Rev. Lett.* **111**, 106601 (2013).
9. Celinski, Z. & Heinrich, B. Ferromagnetic resonance linewidth of Fe ultrathin films grown on a bcc Cu substrate. *J. Appl. Phys.* **70**, 5935 (1991).
10. Yu, H. *et al.* High propagating velocity of spin waves and temperature dependent damping in a CoFeB thin film. *Appl. Phys. Lett.* **100**, 262412 (2012).
11. Neusser, S. & Grundler, D. Magnonics: Spin Waves on the Nanoscale. *Advanced Materials* **21**, 2927–2932 (2009).
12. Sergha, A. A., Chumak, A. V. & Hillebrands, B. YIG magnonics. *J. Phys. D: Appl. Phys.* **43**, 264002 (2010).
13. Nikitov, S. A., Tailhades, Ph. & Tsai, C. S. Spin waves in periodic magnetic structures: magnonic crystals. *J. Magn. Mater.* **236**, 320–330 (2001).
14. Khitun, A., Bao, M. & Wang, K. L. Magnonic logic circuits. *J. Phys. D: Appl. Phys.* **43**, 264005 (2010).
15. Eshaghian-Wilner, M. M., Khitun, A. & Wang, K. L. Spin-wave architectures. *US patent 8193598*, B2 (2012).
16. Gertz, F., Kozhevnikov, A., Filimonov, Y. & Khitun, A. Magnonic holographic memory. *arXiv*: **1401.5133**, (2014).
17. Verba, T. *et al.* Conditions for the spin wave nonreciprocity in an array of dipolarly coupled magnetic nanopillars. *Appl. Phys. Lett.* **103**, 082407 (2013).
18. Schneider, T., Serga, A. A., Neumann, T. & Hillebrands, B. Phase reciprocity of spin-wave excitation by a microstrip antenna. *Phys. Rev. B* **77**, 214411 (2008).
19. Sekiguchi, T. *et al.* Nonreciprocal emission of spin-wave packet in FeNi film. *Appl. Phys. Lett.* **97**, 022508 (2010).
20. Jamali, M., Kwon, J. H., Seo, S., M. Lee, K. J. & Yang, H. Spin wave nonreciprocity for logic device applications. *Sci. Rep.* **3**, 3160 (2013).
21. Sato, N., Sekiguchi, K. & Nozaki, Y. Electrical Demonstration of Spin-Wave Logic Operation. *Applied Physics Express* **6**, 063001 (2013).
22. Perzlmaier, K., Woltersdorf, G. & Back, C. H. Observation of the propagation and interference of spin waves in ferromagnetic thin films. *Phys. Rev. B* **77**, 054425 (2008).
23. Liu, T. *et al.* Ferromagnetic resonance of sputtered yttrium iron garnet nanometer films. *J. Appl. Phys.* **115**, 17A501 (2014).
24. Hahn, C. *et al.* Measurement of the intrinsic damping constant in individual nanodisks of  $\text{Y}_3\text{Fe}_5\text{O}_{12}$  and  $\text{Y}_3\text{Fe}_5\text{O}_{12}$ -Pt. *App. Phys. Lett.* **104**, 152410 (2014).
25. Pirro, P. *et al.* Spin-wave excitation and propagation in microstructured waveguides of yttrium iron garnet/Pt bilayers. *App. Phys. Lett.* **104**, 012402 (2014).
26. Vlaminck, V. & Bailleul, M. Spin-wave transduction at the submicrometer scale: Experiment and modeling. *Phys. Rev. B* **81**, 014425 (2010).
27. Neusser, S. *et al.* Anisotropic propagation and damping of spin waves in a nanopatterned antidot lattice. *Phys. Rev. Lett.* **105**, 067208 (2010).
28. Kalinikos, B. A. & Slavin, A. N. Theory of dipole-exchange spin wave spectrum for ferromagnetic films with mixed exchange boundary conditions. *J. Phys. C: Solid State Phys.* **19**, 7013–7033 (1986).
29. d'Allivy Kelly, O. *et al.* Inverse spin Hall effect in nanometer-thick yttrium iron garnet/Pt system. *App. Phys. Lett.* **103**, 082408 (2014).
30. Edmonds, D. T. & Petersen, R. G. Effective exchange constant in yttrium iron garnet. *Phys. Rev. Lett.* **2**, 12 (1959).
31. Yu, H. *et al.* Omnidirectional spin-wave nanograting coupler. *Nat. Commun.* **4**, 2702 (2013).
32. Demidov, V. E. *et al.* Excitation of microwaveguide modes by a stripe antenna. *Appl. Phys. Lett.* **95**, 112509 (2009).
33. Huber, R. *et al.* Reciprocal Damon-Eshbach-type spin wave excitation in a magnonic crystal due to tunable magnetic symmetry. *App. Phys. Lett.* **102**, 012403 (2013).
34. Chumak, A. V. *et al.* All-linear time reversal by a dynamic artificial crystal. *Nature Commun.* **1**, 141 (2010).
35. Vlaminck, V. & Bailleul, M. Current-induced spin-wave Doppler shift. *Science* **322**, 410–413 (2008).
36. Wu, Y. *et al.* A Three-Terminal Spin-Wave Device for Logic Applications. *J. Nanoelectron. Optoe.* **4**, 394–397 (2009).
37. Kambersky, V. & Patton, C. E. Spin-wave relaxation and phenomenological damping in ferromagnetic resonance. *Phys. Rev. B* **11**, 2668–2672 (1975).
38. Gurevich, A. G. & Melkov, G. A. Magnetization oscillations and waves. *CRC press, Boca Raton* (1996).
39. Duerr, G. Spin Waves in Nanochannels, Created by Individual and Periodic Bi-Component Ferromagnetic Devices. *PhD thesis, Technische Universitaet Muenchen* (2012).
40. Schwarze, T. Spin Waves in 2D and 3D Magnonic Crystals: From Nanostructured Ferromagnetic Materials to Chiral Helimagnets. *PhD thesis, Technische Universitaet Muenchen* (2013).

## Acknowledgments

The authors thank Thomas Schwarze and Filip Lisecki for support. Financial support by the German Excellence Cluster Nanosystems Initiative Munich (NIM), the DFG via project GR1640/5 in the priority programme SPP1538 and ANR-12-ASTR-0023 Trinidad is gratefully acknowledged.

## Author contributions

H.Y. and D.G. planned the experiment, designed the samples and analyzed the data. O.d'A., V.C., R.B., P.B., A.A. and H.Y. fabricated the samples. H.Y. conducted the experiments. F.B., R.H. and I.S. helped to analyze the data. H.Y. and D.G. wrote the manuscript. All authors commented on the manuscript.

## Additional information

**Competing financial interests:** The authors declare no competing financial interests.

**How to cite this article:** Yu, H. *et al.* Magnetic thin-film insulator with ultra-low spin wave damping for coherent nanomagnonics. *Sci. Rep.* **4**, 6848; DOI:10.1038/srep06848 (2014).



This work is licensed under a Creative Commons Attribution-NonCommercial-ShareAlike 4.0 International License. The images or other third party material in this article are included in the article's Creative Commons license, unless indicated otherwise in the credit line; if the material is not included under the Creative Commons license, users will need to obtain permission from the license holder in order to reproduce the material. To view a copy of this license, visit <http://creativecommons.org/licenses/by-nc-sa/4.0/>